

In vivo single-particle imaging of nuclear mRNA export in budding yeast demonstrates an essential role for Mex67p

Carlos Smith,^{1,2*} Azra Lari,^{3*} Carina Patrizia Derrer,^{4*} Anette Ouwehand,^{1,2,5} Ammeret Rossouw,^{1,2,5} Maximiliaan Huisman,^{1,2,5} Thomas Dange,⁵ Mark Hopman,⁵ Aviva Joseph,^{1,2} Daniel Zenklusen,⁶ Karsten Weis,^{4,7} David Grunwald,^{1,2,5} and Ben Montpetit³

¹RNA Therapeutics Institute and ²Department Biochemistry and Molecular Pharmacology, University of Massachusetts Medical School, Worcester, MA 01605

³Department of Cell Biology, University of Alberta, T6G 2H7 Edmonton, Alberta, Canada

⁴Department of Biology, Institute of Biochemistry, ETH Zurich, 8093 Zurich, Switzerland

⁵Bionanoscience, Kavli Institute of Nanoscience, Delft University of Technology, 2628 CJ Delft, Netherlands

⁶Département de Biochimie et Médecine Moléculaire, Université de Montréal, H3T 1J4 Montréal, Québec, Canada

⁷Department of Cell and Developmental Biology, University of California, Berkeley, Berkeley, CA 94720

Many messenger RNA export proteins have been identified; yet the spatial and temporal activities of these proteins and how they determine directionality of messenger ribonucleoprotein (mRNP) complex export from the nucleus remain largely undefined. Here, the bacteriophage PP7 RNA-labeling system was used in *Saccharomyces cerevisiae* to follow single-particle mRNP export events with high spatial precision and temporal resolution. These data reveal that mRNP export, consisting of nuclear docking, transport, and cytoplasmic release from a nuclear pore complex (NPC), is fast (~200 ms) and that upon arrival in the cytoplasm, mRNPs are frequently confined near the nuclear envelope. Mex67p functions as the principal mRNP export receptor in budding yeast. In a *mex67-5* mutant, delayed cytoplasmic release from NPCs and retrograde transport of mRNPs was observed. This proves an essential role for Mex67p in cytoplasmic mRNP release and directionality of transport.

Introduction

In eukaryotes, the physical separation of transcription and translation by the nuclear envelope (NE) allows for additional modes of quality control and regulation to be imposed on the gene expression program and necessitates transport of mRNA from the nucleus to the cytoplasm. Passage across the NE is predominantly mediated by the nuclear pore complex (NPC), which is composed of ~30 nucleoporin proteins (Nups) that together form a channel connecting the nucleoplasm and cytoplasm (Wente and Rout, 2010; Floch et al., 2014). To access this channel, each mRNA must be assembled into an RNP complex with export factors (e.g., Mex67p) to allow a messenger RNP (mRNP) to dock to an NPC, translocate across the NE through the transport channel, and reach the cytoplasm (Niño et al., 2013). During export, mRNPs undergo temporally and spatially ordered remodeling in which certain proteins are removed before export (e.g., Yra1p), whereas others are removed upon arrival in the cytoplasm (e.g., Mex67p and Nab2p). This provides

a mechanism to regulate and impose directionality on the transport process (Lund and Guthrie, 2005; Köhler and Hurt, 2007; Tran et al., 2007; Iglesias et al., 2010; Oeffinger and Zenklusen, 2012; Müller-McNicoll and Neugebauer, 2013). Overall, many proteins have been identified that, as part of an mRNP, are required for nuclear maturation, export, and cytoplasmic release (Müller-McNicoll and Neugebauer, 2013; Niño et al., 2013; Bonnet and Palancade, 2014; Oeffinger and Montpetit, 2015). However, numerous questions remain regarding the assembly and composition of the mRNP and how each protein factor contributes to the export event.

Recent advances in imaging technology (e.g., camera sensitivity and microscope design) and methodology (e.g., RNA-tagging strategies) allow individual mRNAs to be visualized in vivo. The ability to image individual mRNPs in living cells has provided important insight into various aspects of mRNP export, including the first measurements of export kinetics (Grunwald and Singer, 2010; Mor et al., 2010; Siebrasse et al., 2012; Ma et al., 2013). Here, we have applied these meth-

*C. Smith, A. Lari, and C.P. Derrer contributed equally to this paper.

Correspondence to Ben Montpetit: ben.montpetit@ualberta.ca; or David Grunwald: david.grunwald@umassmed.edu; or Karsten Weis: karsten.weis@bc.biol.ethz.ch

Abbreviations used in this paper: CRLB, Cramer-Rao lower bound; MLE, maximum likelihood estimate; mRNP, messenger RNP; NE, nuclear envelope; NPC, nuclear pore complex; Nup, nucleoporin protein; SNR, signal to noise ratio.

© 2015 Smith et al. This article is distributed under the terms of an Attribution–Noncommercial–Share Alike–No Mirror Sites license for the first six months after the publication date (see <http://www.rupress.org/terms>). After six months it is available under a Creative Commons license (Attribution–Noncommercial–Share Alike 3.0 Unported license, as described at <http://creativecommons.org/licenses/by-nc-sa/3.0/>).

ods to single-particle imaging of mRNP export in the budding yeast *Saccharomyces cerevisiae*. The availability of mutants that disrupt yeast mRNP export and NPC function allows us to investigate the kinetics and regulation of mRNP export at the level of a single RNA molecule. Using this approach, we tracked hundreds of mRNPs in living cells, analyzed the kinetics of mRNA export events, and characterized the role of the essential mRNA export factor Mex67p. Our results show that mRNP transport across the NE inside the living cell is fast (~200 ms), well in agreement with prior findings (Grünwald and Singer, 2010; Mor et al., 2010; Siebrasse et al., 2012), and prove a critical role for Mex67p in cytoplasmic mRNP release and directional NPC transport.

Results and discussion

To observe the mRNP export process in living cells, we used the bacteriophage PP7 RNA-labeling system (Chao et al., 2008; Hocine et al., 2013). 24 copies of the PP7 operator sequence were inserted into the 3' UTR of the *GFA1* gene (*GFA1-PP7*), which can be fluorescently labeled when bound by the PP7 coat protein (PP7CP) fused to YFP (Fig. 1 A and Fig. S1 A). *GFA1* is an essential gene involved in chitin synthesis (Watzel and Tanner, 1989) and was selected because its relatively low expression level was suitable for single-particle tracking (Lipson et al., 2009). Like most yeast genes, *GFA1* lacks introns (Rodriguez-Medina and Rymond, 1994; Spingola et al., 1999), and the *GFA1* mRNA is near the mean mRNA length in yeast (2,154 nt vs. ~1,400 nt; Hurowitz and Brown, 2003). The Nup Ndc1p fused to tdTomato was also coexpressed with *GFA1-PP7* and PP7-CP-3xYFP, resulting in the reference (*REF*) strain, in which the position of a *GFA1* mRNP (PP7-CP-3xYFP multiplexed on the PP7 operator) could be determined relative to NPCs (Ndc1p-tdTomato) to track mRNP export (Fig. 1 A).

Previous studies using PP7 and the related MS2 RNA-labeling approach in yeast and metazoan systems have demonstrated that the presence of stem loops in the 3' UTR of a transcript does not alter transcript levels, localization, or RNP assembly (Bertrand et al., 1998; Haim et al., 2007; Hocine et al., 2013; Park et al., 2014; Song et al., 2015). Importantly, the additional sequence in the *GFA1* 3' UTR and fusion of tdTomato to Ndc1p, both essential genes, did not impact growth of the *REF* strain (Fig. S1 B), suggesting that the presence of the operator stem loops, the binding of PP7-CP-3xYFP to the *GFA1-PP7* mRNA, and the tagging of Ndc1p do not significantly affect *GFA1* mRNP biogenesis or overall cellular fitness. We cannot rule out the possibility that the addition of PP7 stem loops might subtly affect the *GFA1* mRNA, as it was recently shown that the presence of MS2 stem loops can interfere with the cytoplasmic degradation of an mRNA by Xrn1p (Garcia and Parker, 2015). However, by focusing on nuclear mRNA export events, our analysis selected for functional mRNPs that were transported across an NPC and were not recognized by nuclear surveillance machinery. To further verify that the PP7 stem loops did not alter steady-state *GFA1* transcript levels, the number of transcripts per cell was determined using single-molecule FISH to be 14 ± 7 in the parental strain (no PP7 stem loops) and 13 ± 6 in the *REF* strain. This suggests that the presence of the PP7 stem loops in the 3' UTR of *GFA1* does not significantly alter steady-state mRNA expression levels ($P = 0.37$; two-tailed t test; $n = 100$ cells; Fig. S1 C).

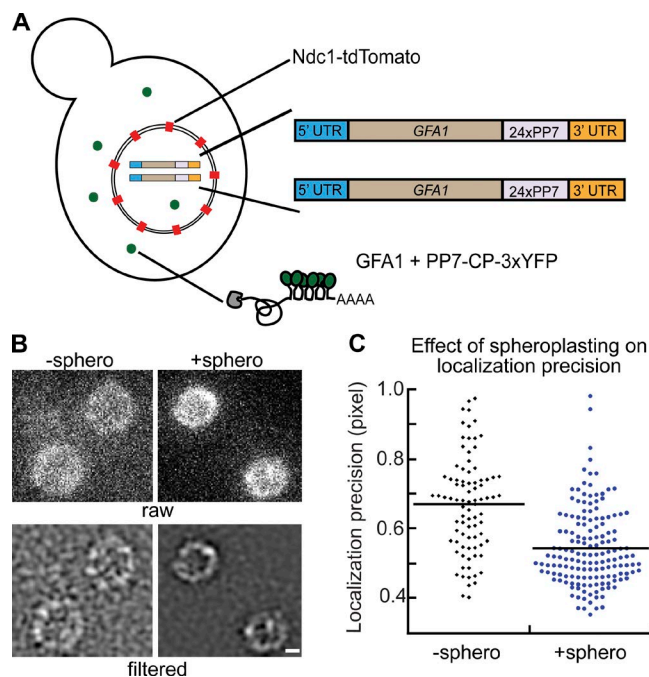


Figure 1. REF strain design and characterization. (A) Schematic displaying features of the yeast strains used to monitor mRNP export. Upon transcription, the *GFA1* mRNA that carries 24xPP7 loops in the 3' UTR is bound by the PP7-CP-3xYFP appearing as particles that can be tracked in relation to NPCs that are marked by Ndc1-tdTomato. (B) Fluorescent images of the Ndc1-tdTomato signal in *REF* cells using identical image acquisition settings showing the improvement in image quality after removal of the yeast cell wall. Examples of both raw and Laplacian filtered images are shown. Bar, 1 μm. (C) Dot plot displaying the localization precision (pixel = 96 nm) obtained when tracking mRNP particles in cells with (–sphero; $n = 86$) and without a cell wall (+sphero; $n = 156$), with the mean denoted by a black line for each.

In the *REF* strain, PP7-CP-YFP-positive particles were predominantly observed in the cytoplasm, as would be expected at steady state, and this is consistent with our *GFA1* single-molecule FISH data. The ability to observe particles was dependent on the presence of PP7 operator loops within the *GFA1* 3' UTR (Fig. S1 A), and most particles were relatively uniform in size and brightness, but some cytoplasmic particles appeared brighter and larger. On occasion, these large particles within the cytoplasm merged and split, suggesting that they may contain multiple mRNAs (Fig. S1 D and Video 1). This could represent the accumulation of decay intermediates in P-bodies (Garcia and Parker, 2015) or other assemblies containing multiple mRNAs, which have recently been reported in live cultured neurons and *S. cerevisiae* (Park et al., 2014; Simpson et al., 2014). Large assemblies were rarely observed in the nucleus of *REF* cells and were not observed to undergo mRNP export.

Measurements of mRNP export kinetics have shown that mRNA export occurs within a few hundred milliseconds and involves discrete steps that include NPC docking, translocation, and cytoplasmic release (Grünwald and Singer, 2010; Siebrasse et al., 2012). Imaging the rapid dynamics of cellular processes, including mRNA export, at the single particle level presents a major challenge (Liu et al., 2015). For instance, information from multiple channels (i.e., mRNA and NPC signals) must be collected concurrently at high frame rates in a manner that maximizes signal to noise ratios (SNRs) and localization precision. To address this challenge, we used an imaging setup capable

of simultaneously capturing two-channel imaging data at high frame rates with precise image registration (see Materials and methods section Live cell imaging of mRNP export and image processing; Grünwald and Singer, 2010). Importantly, complications introduced by system drift or cellular movement (e.g., NPC mobility) are negated by our imaging setup that allows us to monitor the position of both the mRNP and Ndc1p in every frame at the same instance in time.

Still, imaging at the rate required to measure export kinetics (67 Hz in this study) limited photon collection, which, combined with cellular background and light scatter introduced by the yeast cell wall, diminished SNR. To overcome this issue, the yeast cell wall was removed, and cells were imaged in medium containing sorbitol for osmotic support (Fig. 1 B), which substantially increased the SNR (see Materials and methods section Calculation of signal improvements). This resulted in reduced widths (σ) of single-particle signals ($P < 0.01$; Wilcoxon rank-sum test) and a 23% increase in localization precision (Fig. 1 C). Cell wall removal also has the effect of inducing *GFA1* expression for the purpose of cell wall synthesis; consequently, cells with labeled *GFA1* mRNPs became apparent within 15 min after reintroducing growth media, and we were able to collect data for ~90 min before the newly forming cell wall increased the background as a result of light scatter.

Using this approach, we collected two-channel imaging data for 500 frames at 67 Hz from *REF* cells with a measured colocalization precision of 56 ± 20 nm between the two channels (see Materials and methods section Registration and colocalization precision). Because of the small size of yeast, the use of a 1.3 NA objective allowed ~60% of the nuclear volume to be imaged in a single focal plane; thus, mRNP particles could be tracked for significantly more frames than in mammalian cells (Grünwald and Singer, 2010).

In the dataset collected from ~450 *REF* cells, we identified 43 successful mRNP export events. Each event contained a tracked particle, which docked to the nuclear side of the NE and moved in successive frames from the interior of the nucleus to the cytoplasm, where it was released (Fig. 2 A and Videos 2, 3, and 4). We classified mRNPs within every frame as being in one of the following states: nucleoplasmic, nuclear docked, transition between docked states, cytoplasmic docked, or cytoplasmic. Each state was assigned based on the distance between an mRNP and the NE, plus the dynamic behavior (i.e., the direction and distance the particle moved with respect to the NE) of the particle in the preceding and subsequent frames (see Materials and methods section Definition of transport states and data analysis). Using these state values, the duration of an export event was calculated from the time of nuclear docking until mRNP release into the cytoplasm, as previously described (Kubitschek et al., 2005; Dange et al., 2008; Grünwald and Singer, 2010). Using these data, both dwell time analysis (Kubitschek et al., 2005) and maximum likelihood estimate (MLE; Kay, 1993) yielded total mean export times of 188 and 215 ms, respectively (Tables 1 and S1; see Materials and methods section Dwell time estimation). These export times are similar to those reported for transcripts modified with the MS2 RNA-tagging system in mouse cells and for unmodified transcripts labeled by fluorescently tagged mRNP proteins injected into insect salivary gland cells (Grünwald and Singer, 2010; Mor et al., 2010; Siebrasse et al., 2012) but are slower than times reported using single-point edge-excitation subdiffraction microscopy (Ma et al., 2013). Our findings, therefore, indicate

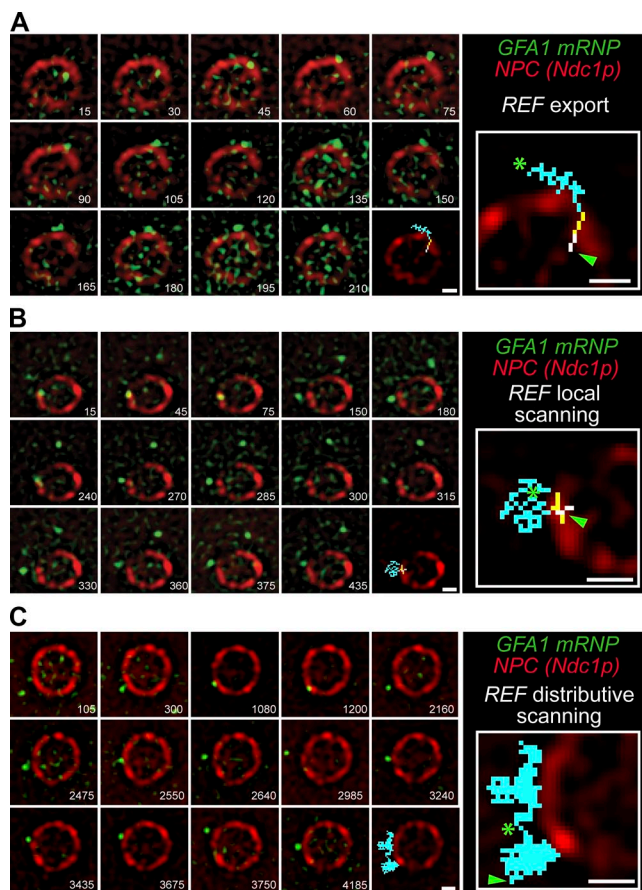


Figure 2. *GFA1* mRNP export and NE scanning in *REF* strain. (A) Merged and registered images show consecutive frames of a successful export event based upon tracking of the tagged *GFA1* mRNP across the NE in the *REF* strain (see Video 2). (B and C) Selected nonconsecutive frames show local (B) and distributive (C) NE scanning interactions between an mRNP and the NE (see Videos 5 and 6, respectively). For all panels, cells were imaged at 26°C and 67 Hz with the time from the start of the event given in the bottom right of each image in milliseconds. The last image and inset show an overlay of the mRNP path that is color coded based on position (white, nuclear docked; yellow, transition; blue, cytoplasmic docked/cytoplasm). Each green arrowhead and star denotes mRNP positions at the beginning and end of the track, respectively. Bars, 1 μ m.

that export in yeast and mammals occur on a similar time scale, consistent with a conservation of the NPC transport mechanism between these species.

During analysis of the *REF* dataset, we noted that mobile *GFA1* mRNPs would remain in close proximity to the NE and repeatedly enter a docked state, which was observed as confinement of mRNPs near the NE (Videos 5 and 6). To quantify this behavior, we used the states defined in our tracking data and counted particles that docked at the NE multiple times, each separated by a state of nucleoplasmic or cytoplasmic diffusion for less than seven frames (105 ms). We termed this behavior “scanning.” NE scanning was predominantly observed in the cytoplasm ($n = 102$), but also occurred infrequently in the nucleus ($n = 4$). NE scanning has also been observed for *MDN1*, *GLT1*, and *CLB2* mRNAs and was shown to be dependent on the nuclear basket components Mlp1p and Mlp2p (see Saroufim et al. in this issue). The low frequency of nuclear scanning suggests that docking of the *GFA1* mRNP to the NE often results in a productive NPC interaction and export. Indeed, we found that ~90% of the mRNPs observed to dock at the NE were

successfully exported (Table 1). The functional significance of nuclear scanning remains unclear, but given the low frequency observed here, this may relate to mRNP quality control mechanisms occurring at NPCs, to limited access of an mRNP to a channel engaged with other cargoes, or to differences in cellular status (Tutucci and Stutz, 2011; Bonnet and Palancade, 2014). In addition, ~35% of successfully exported mRNPs underwent cytoplasmic scanning directly after export. The observed NE scanning frequency after export is likely an underestimate because many tracked particles moved out of focus after arrival in the cytoplasm. Cytoplasmic scanning may therefore be intimately related to the export event.

We could further distinguish two types of cytoplasmic scanning behaviors that confined the mRNP in close proximity to the NE. We observed particles that interacted with the same area of the NE (local scanning; Fig. 2 B and Video 5) or particles that made contacts over a large area of the NE (distributive scanning; Fig. 2 C and Video 6). Local NE scanning may reflect an mRNP remaining engaged with cytoplasmic Nups within the same NPC that facilitated transport. In this case, the apparent distance that the particle is able to travel into the cytoplasm and along the NE would be determined by the ~50-nm distance that NPC fibrils extend into the cytoplasm and the flexibility of an mRNA molecule (Fahrenkrog et al., 1998; Alber et al., 2007). In contrast, distributive NE scanning involves distances far beyond 50 nm, suggesting that an mRNP could make repeated contacts with the NE involving multiple NPCs (Fig. 2 C and Video 6). Both NE scanning behaviors are consistent with repeated interactions between the mRNP and the NE after translocation. Perhaps some export receptors are not immediately removed from mRNPs upon translocation and multiple NPC–mRNP interactions are required for complete remodeling and cytoplasmic release. It will be interesting to learn if mRNP remodeling can be distributed across multiple NPCs and need not occur solely at the NPC that facilitated export. Yet another possibility is that some instances of NE scanning reflect NPC interactions important for events downstream of mRNA export, as a function in translation was proposed for NPC-associated

Dbp5p and the Nup Gle1p (Gross et al., 2007; Bolger et al., 2008; Alcázar-Román et al., 2010; Bolger and Wente, 2011).

Having established an imaging approach in yeast to measure mRNP export kinetics, we examined the impact of a mutant Mex67p protein on nuclear export dynamics of *GFA1* mRNPs. Mex67p (NXF1/TAP in metazoans) is an essential export factor that, as part of the mRNP, interacts with components of the NPC to facilitate export (Segref et al., 1997; Grüter et al., 1998; Santos-Rosa et al., 1998; Katahira et al., 1999; Bachi et al., 2000; Hurt et al., 2000; Strässer et al., 2000; Stutz et al., 2000; Rodrigues et al., 2001; Lund and Guthrie, 2005; Tuck and Tollervey, 2013; Baejen et al., 2014). Together, these works support a model of export where (a) multiple Mex67p molecules bind along the length of mRNA during nuclear maturation, (b) Mex67p promotes mRNP transport through the NPC by binding FG Nups, and (c) Mex67p dissociates from the mRNP on the cytoplasmic face of the NPC, preventing further interactions with the NPC. Displacement of Mex67p would therefore impart directionality on nuclear mRNA export (Stewart, 2007).

We initially imaged cells carrying the temperature-sensitive *mex67-5* allele at the nonpermissive temperature of 37°C (Segref et al., 1997), but mRNPs became static and reduced in number, precluding analysis of export. Consequently, we performed imaging at 26°C, which was also used to collect the *REF* dataset. At 26°C, the *mex67-5* strain did not have observable growth defects or mRNA export defects, as measured using an oligo-dT FISH assay to determine steady-state mRNA localization (Fig. S2, A and B). Using GFP-tagged versions of Mex67p and Mex67-5p, we observed an increased nuclear pool of Mex67-5p at 26°C, but the majority remained at the NE similar to Mex67p. This is in contrast to Mex67-5p localization at 37°C, where foci within both the nucleus and cytoplasm formed (Fig. S2 C; Segref et al., 1997). The mean number of *GFA1* mRNAs observed in the *mex67-5* strain (12 ± 5) by single-molecule FISH was significantly different ($P < 0.05$; two-tailed t test; $n = 100$ cells) than the *REF* strain (14 ± 6 ; Fig. S2 D). The *mex67-5* mutation, therefore, impacts Mex67p localization and *GFA1* mRNA levels, indicating that Mex67-5p has a partial

Table 1. Summary of *GFA1-PP7* mRNP imaging data

	<i>REF</i>	<i>mex67-5</i>
Particles tracked	291	203
Nuclear docking events	47	23
Export events	43	9
Retrograde export events	0	7
Mean export time—dwell time analysis (ms)	188 ^a	ND
Mean export time—MLE (ms)	215 ^a	ND
Mean nuclear docking time during export—dwell time analysis (ms)	32 ^a	362 ^a
Mean nuclear docking time during export—MLE (ms)	39 ^a	202 ^a
Mean transition time during export—dwell time analysis (ms)	87 ^a	406 ^a
Mean transition time during export—MLE (ms)	99 ^a	383 ^a
Mean cytoplasmic docking time during export—dwell time analysis (ms)	62 ^a	1,258 ^a
Mean cytoplasmic docking time during export—MLE (ms)	77 ^a	943 ^a
NE-associated mRNPs per cell	0.2 ± 0.4^b	0.5 ± 0.7^b
Nuclear scanning events	4	2
Cytoplasmic scanning events	102	16

^aExport data underlying dwell time analysis may not have a normal distribution; consequently, an MLE analysis was performed (Kay, 1993). The differences between dwell times in *REF* and *mex67-5* strains were tested using the distribution independent Wilcoxon rank-sum test and were found to be significant at $P < 0.05$ for the transition and cytoplasmic docking states. For more details and a discussion of error measurements, see the Materials and methods section Statistical analyses.

^bStandard deviation.

loss of function at 26°C, but this does not result in significant changes in mRNA distributions at steady state.

By using single-particle imaging, we observed that *GFA1* mRNPs in the *mex67-5* mutant at 26°C were threefold more frequently associated with the NE (Table 1). Data from all tracked mRNPs (i.e., independent of being part of a successful export event) were further used to estimate the length of time a particle spent in a single state (e.g., cytoplasmic docked) before transitioning to the next state (e.g., cytoplasmic). We found that mRNPs in the *mex67-5* strain persisted significantly longer in each of the states ($P < 0.01$; Wilcoxon rank-sum test; Fig. 3 A). The number of cytoplasmic scanning events was also decreased in the *mex67-5* strain (Table 1), and we observed mRNPs in the cytoplasmic docked state for the entire duration of a video (Fig. 3 B and Video 7). These data demonstrate that *Mex67-5p* alters the dynamics of mRNP–NPC binding interactions at 26°C, which can be quantified using our single-particle imaging approach.

In the dataset collected from ~250 *mex67-5* cells, only nine successful mRNP export events were identified (Fig. 4, A and B; and Videos 8 and 9). These ranged in length from 210 to 4,080 ms, and a comparison of successful export times from *REF* and *mex67-5* cells showed a clear bias ($P < 0.01$; Wilcoxon rank-sum test) toward long events in *mex67-5* cells (Fig. 4 B). However, the low number of successful events prevented an accurate calculation of a mean export time. Dwell time analysis of the states occupied by successfully exported mRNPs showed that in *mex67-5* cells, the lengthening of export times was the result of an ~6-fold increase in nuclear docking times, an ~4-fold increase in transition times, and an ~20-fold increase in cytoplasmic docking times when compared with the duration of these states in *REF* export events (Tables 1 and S1). The differences between *REF* and *mex67-5* strains for transition times ($P < 0.01$; Wilcoxon rank-sum test) and cytoplasmic docking times ($P < 0.01$; Wilcoxon rank-sum test) were statistically significant, whereas the 6× increase in nuclear docking times was not ($P > 0.05$; Wilcoxon rank-sum test). These data fit well with the observed increase in NE-associated mRNPs (Table 1), the low number of observed successful export events, and the extended interactions of tracked mRNPs with the NE in *mex67-5* cells (Fig. 3 and Video 7).

Of the nuclear mRNPs that docked with the NE in *mex67-5*, only 32% (9 of 23) were ultimately exported, which contrasted with the *REF* strain, where 90% of nuclear docking events led to export (Table 1). Interestingly, from the 14 particles that did not export, seven retrograde transport events were identified in which mRNPs traverse the NE and achieve a state of cytoplasmic docking before ultimately returning to the nucleoplasm (Fig. 4 C and Video 10). Retrograde mRNP transport was never observed in *REF* cells. Collectively, the seven reimport events and the ~20-fold increase in cytoplasmic dwell times (Tables 1 and S1) during successful export events strongly argue that the *mex67-5* mutant perturbs directional mRNP export and cytoplasmic release.

The *mex67-5* allele contains a histidine-to-tyrosine amino acid substitution at position 400, and previous studies have shown that there is less mRNA associated with *Mex67-5p* as compared with *Mex67p* (Segref et al., 1997; Lund and Guthrie, 2005). Computational models of mRNA export suggest that the efficiency of mRNP export is highly sensitive to both the number and spacing of export factors along an mRNP (Azimi et al., 2014). As such, a reduced number and/or altered spacing

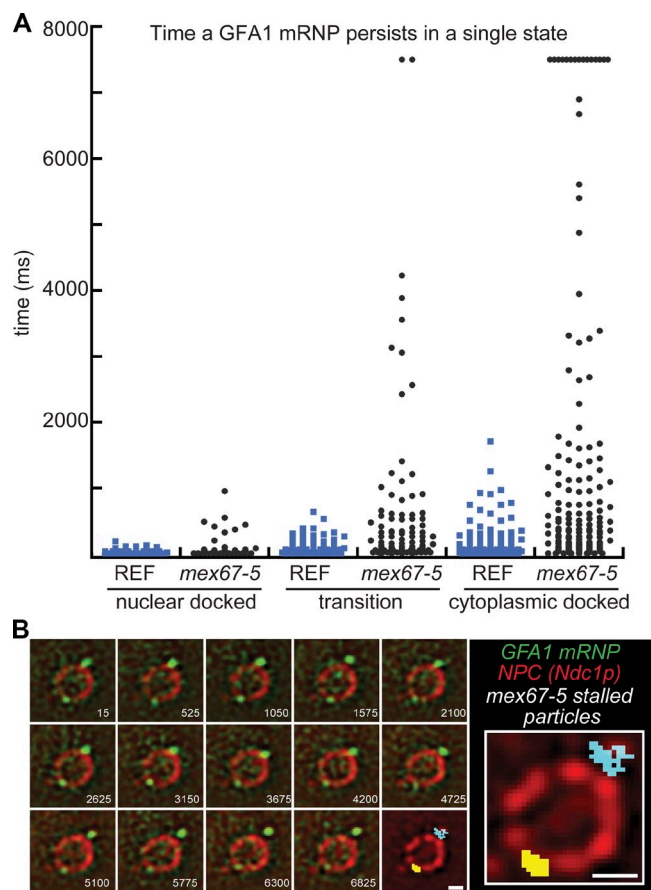


Figure 3. Prolonged *GFA1* mRNP interactions with the NE in *mex67-5*. (A) Dot plot displaying the length of time a *GFA1* mRNP persists in a single state (nuclear docked, transition, or cytoplasmic docked) in *REF* ($n = 49, 82, \text{ and } 108$) and *mex67-5* ($n = 34, 94, \text{ and } 151$) strains. Note that the data presented here use all trace data where a particle interacted with the NE independent of the trace resulting in mRNP export. (B) Selected nonconsecutive frames show the persistent interaction of *GFA1* mRNPs with the NE in *mex67-5* cells (see Video 7). Cells were imaged at 26°C and 67 Hz with the time from the start of the event given in the bottom right of each image in milliseconds. The last image and inset show an overlay of the mRNP path that is color coded based on position (gray, nuclear docked; yellow, transition; blue, cytoplasmic docked/cytoplasm). Bars, 1 μm .

of functional *Mex67p* molecules on the mRNA could lead to changes in mRNP architecture and altered interactions with the NPC that may affect how efficiently the mRNP is transported and remodeled by the NPC. This could explain the resulting inefficiencies and failures in mRNP export reported here, although further work will be required to characterize the molecular basis of these transport defects.

Overall, our work has measured mRNP export kinetics for the first time in *S. cerevisiae* by taking advantage of two powerful experimental systems: single-particle RNA localization microscopy and yeast genetics. Importantly, this approach provides a platform upon which to address fundamental questions related to nuclear mRNA export, including kinetics, regulation, and the mechanisms of transport through NPCs. For example, we have observed the confinement of mRNPs near the NE after arrival in the cytoplasm, suggesting that mRNPs may visit multiple NPCs for the purpose of mRNP remodeling after export. These interactions might function to remodel mRNPs for cytoplasmic release or subsequent events in the mRNA life-cycle (e.g., translation). We have further provided direct evi-

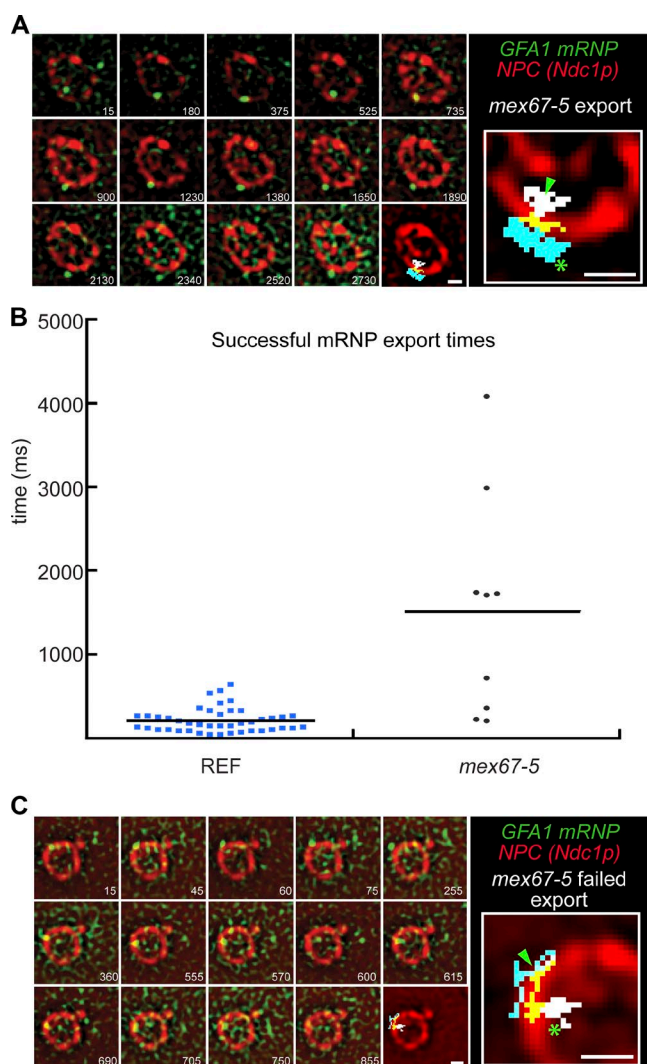


Figure 4. mRNP export kinetics and retrograde transport in *mex67-5*. (A) Merged and registered images show select frames of a successful export event in a *mex67-5* cell (see Video 8). (B) Dot plot showing the distribution of GFA1 mRNP export times in *REF* ($n = 43$) and *mex67-5* ($n = 9$) cells, with the mean denoted by a black line. (C) Selected nonconsecutive frames show a retrograde transport event in which an mRNP on the cytoplasmic side of the NE returns to the nucleus (see Video 10). For A and C, cells were imaged at 26°C and 67 Hz with the time from the start of the event given in the bottom right of each image in milliseconds. The last image and inset show an overlay of the mRNP path that is color coded based on position (white, nuclear docked; yellow, transition; blue, cytoplasmic docked/cytoplasm). Each green arrowhead and star denotes mRNP positions at the beginning and end of the track, respectively. Bars, 1 μ m.

dence for the critical role of Mex67p in imparting directionality to mRNP export. Future applications of our approach will include interrogating the many other proteins involved in mRNP export, including Nups, studies that will be facilitated by the tractable genetics and the expansive knowledge of mRNP export and NPC function in yeast.

Materials and methods

Yeast strain construction

Strains and plasmids used in this study are listed in Tables S2 and S3. To generate imaging strains, a set of 24xPP7 stem loops with a KanMX

selectable marker flanked by loxP sites was integrated into the 3' UTR of the *GFA1* gene using pDZ417 (Hocine et al., 2013) in the diploid yeast strain BY4743 (BYM008). Cre recombinase was expressed from pSH47 (Güldenier et al., 1996) to remove the selectable marker and restore the 3' UTR with the exception of the PP7 loops and a single loxP site. NDC1 was C-terminal tagged in the *GFA1-PP7* heterozygous diploid with tdTomato (Sheff and Thorn, 2004), followed by sporulation and tetrad dissection to isolate a haploid of each mating type that carried *GFA1-PP7* and the Ndc1-tdTomato fusion. The *mex67-5* allele was subsequently integrated into the genome of each haploid using a PCR-based homologous recombination approach, which was confirmed by PCR, temperature sensitivity, and an mRNA export phenotype. Haploids were then mated to form diploids homozygous for the PP7 loops and NDC1 fusion with and without the *mex67-5* allele. Finally, to allow for the visualization of the PP7 containing *GFA1* transcripts, a pRS313-P_{Met25}PP7-CP-3xYFP plasmid (pBM242) was introduced into the diploid strain to generate the *REF* (BYM083) and *mex67-5* (BYM135) strains. To assess growth after PP7 stem loop addition, growth rates were measured for a control strain with no PP7 loops (BYM642) and the *REF* strain (BYM83). Strains were grown overnight in a 24-well plate format with shaking at 26°C, and OD₆₀₀ measurements were performed using the CLARIOstar plate reader (BMG Labtech). The *mex67-5* strain (BYM135) was also assessed for growth defects in comparison with a control strain (BYM129).

GFA1 transcript counting and mRNP NE association

Yeast were grown overnight at 26°C, diluted to an OD₆₀₀ of ~0.1 the next morning, and grown at 26°C to allow at least three doublings. For transcript counting using single-molecule FISH, cells were fixed and GFA1 mRNAs were detected using 48 probes (20mers) directed against GFA1 (BioSearch Technologies) in strains with (BYM83) and without PP7 stem loops (BYM642), as previously described with the noted changes (Hocine et al., 2013). In brief, cells were fixed by the addition of 37% formaldehyde to the cultures (3.7% final concentration) for 30 min at 26°C. Yeast cell walls were digested with Zymolyase (Cedarlane), and spheroplasted cells were applied to 8-well slides coated with poly-L-lysine. Cells were permeabilized using ice-cold methanol for 6 min followed by ice-cold acetone for 30 s. After rehydration and incubation with a hybridization buffer for 1 h at 37°C, 30 μ l of a hybridization buffer containing 20 ng of the GFA1 probes was added to each well and incubated overnight at 37°C. Wells were then washed, and mounting media containing DAPI was added followed by imaging on a microscope (DeltaVision Elite; GE Healthcare) equipped with a front-illuminated scientific complementary metal-oxide (sCMOS) camera driven by softWoRx 6 (GE Healthcare) at 23°C using a 60 \times 1.4 NA oil objective (Olympus).

To determine GFA1 mRNP subcellular localization with respect to the NE, *REF* and *mex67-5* strains were fixed in 2% paraformaldehyde for 15 min, washed with media, and spheroplasted (see the following section). The GFA1 transcript number was determined by manually counting GFA1 foci, and the frequency of NE-associated mRNPs was determined by scoring colocalization between the mRNP (YFP) and NPC (tdTomato) signals. Imaging of both datasets was performed on a microscope (DeltaVision Elite) equipped with a front-illuminated sCMOS camera driven by softWoRx 6 (GE Healthcare) at 23°C using a 60 \times 1.4 NA oil objective (Olympus). Before analysis, images were deconvolved in softWoRx 6 and processed in ImageJ (National Institutes of Health). Specifically, images were adjusted for brightness and contrast, background subtraction was performed, and a Gaussian blur 3D filter was applied.

Live cell imaging of mRNP export and image processing

The overall system design and methodology for imaging was as previously described with the exceptions noted below (Grünwald and Singer,

2010). In brief, imaging was performed on a custom dual channel setup using a 60× 1.3 NA silicone oil immersion objective (refractive index 1.405; Olympus) combined with 500-mm focal length tube lenses, resulting in an effective 167× magnification and 95.8-nm-sized pixel with the emission split in the primary beam path onto two electron-multiplying charge-coupled devices (DU897 BI; iXon; Andor Technology). For excitation of fluorescent proteins, solid-state 514- and 561-nm laser lines (SE; Cobolt) were used, and intensity and on/off were controlled by an acousto-optic tunable filter (AA Opto-Electronics). Simultaneous imaging of NPCs and mRNPs was performed using subframes (approximately two fifths of each chip, 200 × 200 pixel) on both cameras at a frame rate of 67 Hz, equaling a time resolution of 15 ms.

Before imaging, cells were grown overnight at 26°C in synthetic complete media lacking histidine with methionine at 150 mg/liter, diluted to an OD₆₀₀ of 0.1 the next morning, and grown at 26°C to allow at least three doublings. To remove the cell wall, ~2 ODs of cells were collected by centrifugation, washed with water, and resuspended in 50-mM Tris, pH 9.5, and 10-mM DTT solution at room temperature for 15 min. Cells were then collected and resuspended in a 0.3-ml spheroplast buffer (150-mM KPO₄, pH 7.5, 1-mM MgCl₂, and 250 µg/ml Zymolyase) and incubated at 26°C for 45 min. Cells were then placed in 35-mm glass-bottom dishes (MatTek Corporation), coated with concanavalin A (Sigma-Aldrich), and centrifuged at 500 g for 3 min to adhere cells. Unadhered cells were removed by washing with media containing 1.2-M sorbitol and left to recover in 2 ml of fresh media for 30 min at 26°C before imaging. For each cell, four datasets, two in each color, were acquired. First, a registration image was recorded for 375 ms, automatically saved, and 500 ms later, the tracking dataset was recorded for 7.5 s (500 frames) in parallel for both channels.

All image processing for visual analysis was done using Fiji (Schindelin et al., 2012). First, each dataset was tested for drift during acquisition by creating 10 mean projections of 50 frames of the NPC channel video that were normalized and fused into a color-coded hyperstack. Color separation in the resulting stack indicated drift, and these datasets were discarded. Second, in the registration images, the tdTomato signal of Ndc1 was made visible in both channels using “cross-talk on demand” by using 10× more excitation power from the 561-nm laser than for the tracking videos. Using the sensitivity of our electron-multiplying charge-coupled device cameras and the surface reflection of the dichroic, the NPC signal was visible in both the mRNA (one image taken for 375 ms) and the NPC channel (25 images in 375 ms, the mean time projected for analysis). The mRNA and NPC signals were fine-registered postexperimentally by shifting the NPC channel registration image onto the mRNA channel registration image to calculate the parameters to be used for registration of the tracking videos (Preibisch et al., 2009). To make this alignment more robust, the mRNA channel registration image was filtered with a Gaussian kernel (1.5 pixel width) before registration. RGB images of the two registration images before and after registration were saved and visually compared if the correlation factor of the linear shift was better than 0.95. Registration failed at a frequency of ~50%, which we attribute to aberrations caused by heterogeneity in spheroplasting and, at later times, because of rebuilding of the cell wall. The resulting registration precision was determined to be 0.14 pixel, corresponding to 14 ± 17 nm. After these initial quality checks, we created two copies of each tracking video (NPC and mRNA channel), one being the raw data for quantitative image analysis and the other being enhanced for visual inspection. Raw data images were always displayed next to the enhanced images during subsequent visual analysis, and all traces of interest were double checked in the raw dataset to prevent a false positive event identification as a result of image processing. Tracking was done as described previously (Grünwald and Singer, 2010) using a supported

fit routine where signals were identified visually in either the filtered or raw image, and the routine would execute a center of mass within 5 pixels around the click position to identify the coordinate for a 2D Gaussian fit. All fits were done in raw data and all fit parameters and initiation parameters reported to the user. For enhancement of images for visual inspection, we used running mean and a subtraction of a Laplacian filter for the NPC channel and a Laplacian filter for the RNA channel. The kernel size was set relative to the theoretical width of the emission point spread function, and contrast was adjusted in the final RGB videos after processing. After filtering, the transition matrix was applied to the NPC channel video to overlay it onto the mRNA channel video.

Calculation of signal improvements

We quantify an increase or decrease in signal improvement as a change in the mean estimated localization precision. The smallest localization precision possible can be calculated using the Cramer-Rao lower bound (CRLB) and is attained using MLE (Smith et al., 2010). The CRLB depends on the width of the point spread function, the intensity of the single molecule, and the background fluorescence. To quantify the signal improvement, we estimated these parameters in addition to assessing the location of each mRNP and calculated the corresponding CRLB (Smith et al., 2010). These calculations were performed based on mRNP signals from cells with ($n = 86$) and without ($n = 156$) a cell wall, and the localization precision was determined to be 64 ± 13 versus 52 ± 11 nm before and after cell wall removal. Note that total improvement in localization precision was 23% and the shape of the localization distributions significantly changed (Fig. 1 C).

Registration and colocalization precision

The registration precision between channels of 14 nm was determined by calculating the remaining offset between the registration data after linear translation. We chose the rather conservative linear registration model, as the quality of the registration data does not reach the level of individual pores (Grünwald and Singer, 2010). The SD using this method is in the order of the mean. As a result, we do not report spatial binding site distributions, arguing that our total measurement precision is similar to the width of the expected binding site distributions. For kinetic analysis, we use five classification states, but it is important to note that a four-state model also strongly supports our findings. Colocalization precision is given by the square root of the sum of the squared localization (54 nm) and registration precision (14 nm) values and is 56 nm. From binding profiles of β -actin mRNA at the NPC, we know the peak binding sites on the cytoplasmic and nucleoplasmic surface for mRNA transporting within ~200 ms to be 275 nm apart (Grünwald and Singer, 2010).

Definition of transport states and data analysis

Data analysis was performed using a manual tracking interface in which the filtered and raw data were presented simultaneously and a particle of interest was tracked by consecutively clicking through image frames. The maximal displacement from frame to frame was displayed in the tracking channel to identify situations where two particles could be interchanged. In such cases, tracking was ended and the track dismissed. During manual tracking, a descriptive state was assigned to the particle in each frame based on the distance from the NE using the following guidelines: nuclear/cytoplasmic diffusion if the distance was >250 nm, nuclear/cytoplasmic docked if the distance was between 250 and 100 nm, and transition if the distance was <100 nm. The dynamic behavior of the particle (i.e., the direction and distance the particle moved with respect to the NE) in prior and subsequent frames was also used to inform state decisions. Using these descriptors, an analysis was performed in MatLab (MathWorks) using routines to

search for specific events (e.g., export or scanning) based on these five states. We can make this classification because the localization precision of single molecules follows a Gaussian distribution described by $\theta - \hat{\theta} \sim N(0, C(\theta))$, where $\theta = (x, y, I, bg)$, $\hat{\theta}$ is the corresponding MLE, and $C(\theta)$ is CRLB (Kay, 1993). Using our current techniques, we have a total colocalization precision of 56 nm. C_{do} and N_{do} are 275 nm apart, and therefore we can calculate the false classification probability of a C_{do} being an N_{do} event (and the other way around) as $P(C_{do} | N_{do}) = 1 - \text{normcdf}(x = 135, \mu = 0, \sigma = 56)$ that defines the false classification rate as 0.01, or a 0.5% error to each side. When using $P(T | N_{do}, C_{do})$, this increases to 0.23 or an 11.5% error to each side ($2(1 - \text{normcdf}(135/2, 0, 56))$). For a distance of 200 nm between the peak positions $P(C_{do}, N_{do} | T)$, this becomes 37% compared with 7% for $P(C_{do} | N_{do})$. In other words, we are able to describe a two-state (C_{do} - N_{do}) model at the NPC (four states in total, with the diffusive nuclear and cytoplasmic states) with very high confidence (<0.5% error), whereas for a three-state model (C_{do} - T - N_{do}) at the NPC (five states in total), the classification of the transition state has an error probability between 10 and 17% on each side based on our obtained localization precision. As the transition state T is a shift in between docking states, its identification is partially based on our knowledge about the past and future of the particle within the trace. Therefore, we have included the transition state description, but note the related error, which does not impact the major findings of this work related to cytoplasmic docking differences in *mex67-5*.

Dwell time estimation

Because of the limited number of observations, we estimated dwell times using two methods, the dwell time fit based on the histogram (exponential distribution) and an MLE based on the assumption that the data follow an exponential distribution (Colquhoun and Hawkes, 1982; Kubitscheck et al., 2005). In the first method, (a) a histogram is constructed from all the observed dwell times, (b) the histogram is smoothed using a uniform filter having a width of 10 frames, (c) inverted cumulative distribution is constructed (Kubitscheck et al., 2005), and (d) a least squares fit is performed on the histogram. The second approach is an MLE (Kay, 1993). The transport times per condition are assumed to be an independently identical set of random variables having an exponential distribution. The probability density function of observing a dwell time x_j is given by

$$f(x_j; \lambda) = \begin{cases} \lambda e^{-\lambda x_j} & x_j \geq 0 \\ 0 & x_j < 0 \end{cases},$$

where the mean dwell time is equal to λ^{-1} . The likelihood of a sequence of observed dwell times is given by

$$L(\lambda) = \prod_{j=1}^n \lambda e^{-\lambda x_j},$$

and the value for $\hat{\lambda}$ that maximizes the likelihood is given by

$$\hat{\lambda} = \frac{n}{\sum_{j=1}^n x_j}.$$

In both cases, based on the data having an exponential distribution, SD is equal to the mean.

mex67-5 strain characterization

To assay for mRNA export defects, FISH against poly(A)-RNA was performed as previously described (Cole et al., 2002). In brief, *REF* (BMY83) and *mex67-5* (BMY135) strains were grown to mid-log phase at a permissive temperature (26°C) and then shifted to a nonper-

missive (37°C) temperature for 30 min with prewarmed media. After fixation, poly(A)-RNA was detected using a fluorescein-labeled dT₅₀ probe, and DNA was visualized using DAPI. Imaging was performed on a microscope (DeltaVision Elite) equipped with a front-illuminated sCMOS camera driven by softWoRx 6 at 23°C using a 60× 1.4 NA oil objective. To localize Mex67p, haploid strains were generated (KWY5566 and KWY5567) expressing Ndc1p-tdTomato, *GFA1-PP7*, and GFP-tagged Mex67. To avoid cross talk from the PP7-CP tagged with YFP, we used strains that did not express the coat protein. Cells were grown in a synthetic complete medium at 26°C and then imaged in a 384-well plate coated with concanavalin A at 26°C using an inverted epifluorescence microscope (Ti; Nikon) equipped with a Spectra X LED light source and an sCMOS camera (Flash 4.0; Hamamatsu Photonics) using a 100× Plan-Apo 1.4 NA objective and the NIS Elements software (Nikon). All image processing was done using Fiji (Schindelin et al., 2012).

Statistical analyses

Reported p-values were calculated using either *t* tests or Wilcoxon rank-sum tests. The latter can be used in place of *t* tests when it cannot be assumed that the population is distributed normally (Gibbons and Chakraborti, 2011). For all results, the test used is stated in the text.

In analyzing transition times across the NE, the shape of the distribution determines the interpretation of the SD or SEM reported. Although often associated with the symmetric interval of errors around normal distributed data, the SD or SEM can also be used to report on nonnormal distributed data. In this case, the interpretation is based on Chebyshev's theorem specifying that no more than $1/k^2$ fraction of values can be more than k SDs away from the mean. In case of an exponential distribution, this translates into the SD being equal to the mean. In our case, the cumulative distribution of translocation times is equal to the cumulative distribution function of an exponential distribution, as expected (Colquhoun and Hawkes, 1982; Kubitscheck et al., 2005), or arrival time distributions in general. Because of the limited number of observations, we estimate the dwell time using two methods, the dwell time fit based on the histogram (exponential distribution) and an MLE based on the assumption of the data after an exponential distribution. For exponential distributions, the SD is expected to be equal to the mean. Note that a limited amount of data underlies some of the values in Tables 1 and S1 and that the error reported in Table S1 is the error of the measurement.

Online supplemental material

Fig. S1 contains data on the characterization of the PP7-RNA labeling system in *REF* cells, which includes growth rates, GFA1 transcript levels, and particle splitting in the cytoplasm (see Video 1). Fig. S2 shows data on the characterization of *mex67-5* cells at 26°C, which includes growth rates, GFA1 transcript levels, Mex67p localization, and mRNA export status. Video 1 shows *GFA1* mRNP observed to split and merge. Videos 2, 3, and 4 show successful *GFA1* mRNP export events in *REF* cells. Videos 5 and 6 show *GFA1* mRNPs scanning the cytoplasmic side of the NE. Video 7 shows extended mRNP interactions with the NE in *mex67-5*. Videos 8 and 9 show successful *GFA1* mRNP export events in *mex67-5* cells. Video 10 shows a retrograde mRNP transport event in a *mex67-5* cell. Table S1 contains dwell time analysis data, including error measurements for successful mRNP export events. Tables S2 and S3 list strains and plasmids used in this study. Online supplemental material is available at <http://www.jcb.org/cgi/content/full/jcb.201503135/DC1>.

Acknowledgments

We would like to thank members past and present from the Weis, Singer, Grunwald, and Montpetit laboratories for their support of this

work. The Grunwald laboratory moved during this project from the Department of Bionanoscience at Delft University of Technology, where experimental data were acquired, to the RNA Therapeutics Institute at the University of Massachusetts Medical School, where analysis was done.

D. Grunwald thanks Robert H. Singer for initial support of the project through National Institutes of Health grant GM57071 (awarded to R.H. Singer), and for his generous support in transition out of the R.H. Singer laboratory and thereafter. A. Ouwehand, M. Huisman, and D. Grunwald also thank R.H. Singer for hosting in his laboratory at the Howard Hughes Medical Institute Janelia campus. This research was undertaken, in part, thanks to funding from the Canadian Institutes of Health Research (MOP130231 to B. Montpetit), the National Institutes of Health (GM058065 to K. Weis), the Canada Research Chairs program (B. Montpetit), and an Alberta Innovates Technology Futures Graduate Scholarship (A. Lari).

The authors declare no competing financial interests.

Submitted: 30 March 2015

Accepted: 17 September 2015

References

- Alber, F., S. Dokudovskaya, L.M. Veenhoff, W. Zhang, J. Kipper, D. Devos, A. Suprpto, O. Karni-Schmidt, R. Williams, B.T. Chait, et al. 2007. The molecular architecture of the nuclear pore complex. *Nature*. 450:695–701. <http://dx.doi.org/10.1038/nature06405>
- Alcázar-Román, A.R., T.A. Bolger, and S.R. Wente. 2010. Control of mRNA export and translation termination by inositol hexakisphosphate requires specific interaction with Gle1. *J. Biol. Chem.* 285:16683–16692. <http://dx.doi.org/10.1074/jbc.M109.082370>
- Azimi, M., E. Bulat, K. Weis, and M.R.K. Mofrad. 2014. An agent-based model for mRNA export through the nuclear pore complex. *Mol. Biol. Cell.* 25:3643–3653. <http://dx.doi.org/10.1091/mbc.E14-06-1065>
- Bachi, A., I.C. Braun, J.P. Rodrigues, N. Panté, K. Ribbeck, C. von Kobbe, U. Kutay, M. Wilm, D. Görlich, M. Carmo-Fonseca, and E. Izaurralde. 2000. The C-terminal domain of TAP interacts with the nuclear pore complex and promotes export of specific CTE-bearing RNA substrates. *RNA*. 6:136–158. <http://dx.doi.org/10.1017/S1355838200991994>
- Baejen, C., P. Torkler, S. Gressel, K. Essig, J. Söding, and P. Cramer. 2014. Transcriptome maps of mRNP biogenesis factors define pre-mRNA recognition. *Mol. Cell.* 55:745–757. <http://dx.doi.org/10.1016/j.molcel.2014.08.005>
- Bertrand, E., P. Chartrand, M. Schaefer, S.M. Shenoy, R.H. Singer, and R.M. Long. 1998. Localization of ASH1 mRNA particles in living yeast. *Mol. Cell.* 2:437–445. [http://dx.doi.org/10.1016/S1097-2765\(00\)80143-4](http://dx.doi.org/10.1016/S1097-2765(00)80143-4)
- Bolger, T.A., and S.R. Wente. 2011. Gle1 is a multifunctional DEAD-box protein regulator that modulates Ded1 in translation initiation. *J. Biol. Chem.* 286:39750–39759. <http://dx.doi.org/10.1074/jbc.M111.299321>
- Bolger, T.A., A.W. Folkman, E.J. Tran, and S.R. Wente. 2008. The mRNA export factor Gle1 and inositol hexakisphosphate regulate distinct stages of translation. *Cell*. 134:624–633. <http://dx.doi.org/10.1016/j.cell.2008.06.027>
- Bonnet, A., and B. Palancade. 2014. Regulation of mRNA trafficking by nuclear pore complexes. *Genes (Basel)*. 5:767–791.
- Chao, J.A., Y. Patskovsky, S.C. Almo, and R.H. Singer. 2008. Structural basis for the coevolution of a viral RNA-protein complex. *Nat. Struct. Mol. Biol.* 15:103–105. <http://dx.doi.org/10.1038/nsmb1327>
- Cole, C.N., C.V. Heath, C.A. Hodge, C.M. Hammell, and D.C. Amberg. 2002. Analysis of RNA export. *Methods Enzymol.* 351:568–587. [http://dx.doi.org/10.1016/S0076-6879\(02\)51869-3](http://dx.doi.org/10.1016/S0076-6879(02)51869-3)
- Colquhoun, D., and A.G. Hawkes. 1982. On the stochastic properties of bursts of single ion channel openings and of clusters of bursts. *Philos. Trans. R. Soc. Lond. B Biol. Sci.* 300:1–59. <http://dx.doi.org/10.1098/rstb.1982.0156>
- Dange, T., D. Grünwald, A. Grünwald, R. Peters, and U. Kubitscheck. 2008. Autonomy and robustness of translocation through the nuclear pore complex: a single-molecule study. *J. Cell Biol.* 183:77–86. <http://dx.doi.org/10.1083/jcb.200806173>
- Fahrenkrog, B., E.C. Hurt, U. Aebi, and N. Panté. 1998. Molecular architecture of the yeast nuclear pore complex: localization of Nsp1p subcomplexes. *J. Cell Biol.* 143:577–588. <http://dx.doi.org/10.1083/jcb.143.3.577>
- Floch, A.G., B. Palancade, and V. Doye. 2014. Fifty years of nuclear pores and nucleocytoplasmic transport studies: multiple tools revealing complex rules. *Methods Cell Biol.* 122:1–40. <http://dx.doi.org/10.1016/B978-0-12-417160-2.00001-1>
- Garcia, J.F., and R. Parker. 2015. MS2 coat proteins bound to yeast mRNAs block 5' to 3' degradation and trap mRNA decay products: implications for the localization of mRNAs by MS2-MCP system. *RNA*. 21:1393–1395. <http://dx.doi.org/10.1261/rna.051797.115>
- Gibbons, J.D., and S. Chakraborti. 2011. Nonparametric statistical inference. International Encyclopedia of Statistical Science. Springer Berlin Heidelberg, Berlin. 977–979. http://dx.doi.org/10.1007/978-3-642-04898-2_420
- Gross, T., A. Siepmann, D. Sturm, M. Windgassen, J.J. Scarcelli, M. Seedorf, C.N. Cole, and H. Krebber. 2007. The DEAD-box RNA helicase Dbp5 functions in translation termination. *Science*. 315:646–649. <http://dx.doi.org/10.1126/science.1134641>
- Grünwald, D., and R.H. Singer. 2010. In vivo imaging of labelled endogenous β -actin mRNA during nucleocytoplasmic transport. *Nature*. 467:604–607. <http://dx.doi.org/10.1038/nature09438>
- Grüter, P., C. Tabernero, C. von Kobbe, C. Schmitt, C. Saavedra, A. Bachi, M. Wilm, B.K. Felber, and E. Izaurralde. 1998. TAP, the human homolog of Mex67p, mediates CTE-dependent RNA export from the nucleus. *Mol. Cell*. 1:649–659. [http://dx.doi.org/10.1016/S1097-2765\(00\)80065-9](http://dx.doi.org/10.1016/S1097-2765(00)80065-9)
- Güldener, U., S. Heck, T. Fielder, J. Beinbauer, and J.H. Hegemann. 1996. A new efficient gene disruption cassette for repeated use in budding yeast. *Nucleic Acids Res.* 24:2519–2524. <http://dx.doi.org/10.1093/nar/24.13.2519>
- Haim, L., G. Zipor, S. Aronov, and J.E. Gerst. 2007. A genomic integration method to visualize localization of endogenous mRNAs in living yeast. *Nat. Methods*. 4:409–412.
- Hocine, S., P. Raymond, D. Zenklusen, J.A. Chao, and R.H. Singer. 2013. Single-molecule analysis of gene expression using two-color RNA labeling in live yeast. *Nat. Methods*. 10:119–121. <http://dx.doi.org/10.1038/nmeth.2305>
- Hurowitz, E.H., and P.O. Brown. 2003. Genome-wide analysis of mRNA lengths in *Saccharomyces cerevisiae*. *Genome Biol.* 5:R2. <http://dx.doi.org/10.1186/gb-2003-5-1-r2>
- Hurt, E., K. Strässer, A. Segref, S. Bailer, N. Schlaich, C. Presutti, D. Tollervey, and R. Jansen. 2000. Mex67p mediates nuclear export of a variety of RNA polymerase II transcripts. *J. Biol. Chem.* 275:8361–8368. <http://dx.doi.org/10.1074/jbc.275.12.8361>
- Iglesias, N., E. Tutucci, C. Gwizdek, P. Vinciguerra, E. Von Dach, A.H. Corbett, C. Dargemont, and F. Stutz. 2010. Ubiquitin-mediated mRNP dynamics and surveillance prior to budding yeast mRNA export. *Genes Dev.* 24:1927–1938. <http://dx.doi.org/10.1101/gad.583310>
- Katahira, J., K. Strässer, A. Podtelejnikov, M. Mann, J.U. Jung, and E. Hurt. 1999. The Mex67p-mediated nuclear mRNA export pathway is conserved from yeast to human. *EMBO J.* 18:2593–2609. <http://dx.doi.org/10.1093/emboj/18.9.2593>
- Kay, S.M. 1993. Fundamentals of Statistical Signal Processing, Volume I: Estimation Theory. Prentice Hall, Upper Saddle River, NJ. 625 pp.
- Köhler, A., and E. Hurt. 2007. Exporting RNA from the nucleus to the cytoplasm. *Nat. Rev. Mol. Cell Biol.* 8:761–773. <http://dx.doi.org/10.1038/nrm2255>
- Kubitscheck, U., D. Grünwald, A. Hoekstra, D. Rohleder, T. Kues, J.P. Siebrasse, and R. Peters. 2005. Nuclear transport of single molecules: dwell times at the nuclear pore complex. *J. Cell Biol.* 168:233–243. <http://dx.doi.org/10.1083/jcb.200411005>
- Lipson, D., T. Raz, A. Kieu, D.R. Jones, E. Giladi, E. Thayer, J.F. Thompson, S. Letovsky, P. Milos, and M. Causey. 2009. Quantification of the yeast transcriptome by single-molecule sequencing. *Nat. Biotechnol.* 27:652–658. <http://dx.doi.org/10.1038/nbt.1551>
- Liu, Z., L.D. Lavis, and E. Betzig. 2015. Imaging live-cell dynamics and structure at the single-molecule level. *Mol. Cell*. 58:644–659. <http://dx.doi.org/10.1016/j.molcel.2015.02.033>
- Lund, M.K., and C. Guthrie. 2005. The DEAD-box protein Dbp5p is required to dissociate Mex67p from exported mRNPs at the nuclear rim. *Mol. Cell*. 20:645–651. <http://dx.doi.org/10.1016/j.molcel.2005.10.005>
- Ma, J., Z. Liu, N. Michelotti, S. Pitchiaya, R. Veerapaneni, J.R. Androsavich, N.G. Walter, and W. Yang. 2013. High-resolution three-dimensional mapping of mRNA export through the nuclear pore. *Nat. Commun.* 4:1–9. <http://dx.doi.org/10.1038/ncomms3414>
- Mor, A., S. Suliman, R. Ben-Yishay, S. Yunger, Y. Brody, and Y. Shav-Tal. 2010. Dynamics of single mRNP nucleocytoplasmic transport and export

- through the nuclear pore in living cells. *Nat. Cell Biol.* 12:543–552. <http://dx.doi.org/10.1038/ncb2056>
- Müller-McNicoll, M., and K.M. Neugebauer. 2013. How cells get the message: dynamic assembly and function of mRNA-protein complexes. *Nat. Rev. Genet.* 14:275–287. <http://dx.doi.org/10.1038/nrg3434>
- Niño, C.A., L. Hérisant, A. Babour, and C. Dargemont. 2013. mRNA nuclear export in yeast. *Chem. Rev.* 113:8523–8545. <http://dx.doi.org/10.1021/cr400002g>
- Oeffinger, M., and B. Montpetit. 2015. Emerging properties of nuclear RNP biogenesis and export. *Curr. Opin. Cell Biol.* 34:46–53. <http://dx.doi.org/10.1016/j.ceb.2015.04.007>
- Oeffinger, M., and D. Zenklusen. 2012. To the pore and through the pore: a story of mRNA export kinetics. *Biochim. Biophys. Acta.* 1819:494–506. <http://dx.doi.org/10.1016/j.bbagr.2012.02.011>
- Park, H.Y., H. Lim, Y.J. Yoon, A. Follenzi, C. Nwokafor, M. Lopez-Jones, X. Meng, and R.H. Singer. 2014. Visualization of dynamics of single endogenous mRNA labeled in live mouse. *Science.* 343:422–424. <http://dx.doi.org/10.1126/science.1239200>
- Preibisch, S., S. Saalfeld, and P. Tomancak. 2009. Globally optimal stitching of tiled 3D microscopic image acquisitions. *Bioinformatics.* 25:1463–1465. <http://dx.doi.org/10.1093/bioinformatics/btp184>
- Rodrigues, J.P., M. Rode, D. Gatfield, B.J. Blencowe, M. Carmo-Fonseca, and E. Izaurralde. 2001. REF proteins mediate the export of spliced and unspliced mRNAs from the nucleus. *Proc. Natl. Acad. Sci. USA.* 98:1030–1035. <http://dx.doi.org/10.1073/pnas.98.3.1030>
- Rodriguez-Medina, J.R., and B.C. Rymond. 1994. Prevalence and distribution of introns in non-ribosomal protein genes of yeast. *Mol. Gen. Genet.* 243:532–539. <http://dx.doi.org/10.1007/BF00284201>
- Santos-Rosa, H., H. Moreno, G. Simos, A. Segref, B. Fahrenkrog, N. Panté, and E. Hurt. 1998. Nuclear mRNA export requires complex formation between Mex67p and Mtr2p at the nuclear pores. *Mol. Cell. Biol.* 18:6826–6838. <http://dx.doi.org/10.1128/MCB.18.11.6826>
- Saroufim, M.A., P. Bensidoun, P. Raymond, S. Rahman, M.R. Krause, M. Oeffinger, and D. Zenklusen. 2015. The nuclear basket mediates perinuclear mRNA scanning in budding yeast. *J. Cell Biol.* <http://dx.doi.org/10.1083/jcb.201503070>
- Schindelin, J., I. Arganda-Carreras, E. Frise, V. Kaynig, M. Longair, T. Pietzsch, S. Preibisch, C. Rueden, S. Saalfeld, B. Schmid, et al. 2012. Fiji: an open-source platform for biological-image analysis. *Nat. Methods.* 9:676–682. <http://dx.doi.org/10.1038/nmeth.2019>
- Segref, A., K. Sharma, V. Doye, A. Hellwig, J. Huber, R. Lührmann, and E. Hurt. 1997. Mex67p, a novel factor for nuclear mRNA export, binds to both poly(A)⁺ RNA and nuclear pores. *EMBO J.* 16:3256–3271. <http://dx.doi.org/10.1093/emboj/16.11.3256>
- Sheff, M.A., and K.S. Thorn. 2004. Optimized cassettes for fluorescent protein tagging in *Saccharomyces cerevisiae*. *Yeast.* 21:661–670. <http://dx.doi.org/10.1002/yea.1130>
- Siebrasse, J.P., T. Kaminski, and U. Kubitschek. 2012. Nuclear export of single native mRNA molecules observed by light sheet fluorescence microscopy. *Proc. Natl. Acad. Sci. USA.* 109:9426–9431. <http://dx.doi.org/10.1073/pnas.1201781109>
- Simpson, C.E., J. Lui, C.J. Kershaw, P.F.G. Sims, and M.P. Ashe. 2014. mRNA localization to P-bodies in yeast is bi-phasic with many mRNAs captured in a late Bfr1p-dependent wave. *J. Cell Sci.* 127:1254–1262. <http://dx.doi.org/10.1242/jcs.139055>
- Smith, C.S., N. Joseph, B. Rieger, and K.A. Lidke. 2010. Fast, single-molecule localization that achieves theoretically minimum uncertainty. *Nat. Methods.* 7:373–375. <http://dx.doi.org/10.1038/nmeth.1449>
- Song, T., Y. Zheng, Y. Wang, Z. Katz, X. Liu, S. Chen, R.H. Singer, and W. Gu. 2015. Specific interaction of KIF11 with ZBP1 regulates the transport of β -actin mRNA and cell motility. *J. Cell Sci.* 128:1001–1010. <http://dx.doi.org/10.1242/jcs.161679>
- Spingola, M., L. Grate, D. Haussler, and M. Ares Jr. 1999. Genome-wide bioinformatic and molecular analysis of introns in *Saccharomyces cerevisiae*. *RNA.* 5:221–234. <http://dx.doi.org/10.1017/S1355838299981682>
- Stewart, M. 2007. Ratcheting mRNA out of the nucleus. *Mol. Cell.* 25:327–330. <http://dx.doi.org/10.1016/j.molcel.2007.01.016>
- Strässer, K., J. Bassler, and E. Hurt. 2000. Binding of the Mex67p/Mtr2p heterodimer to FXFG, GLFG, and FG repeat nucleoporins is essential for nuclear mRNA export. *J. Cell Biol.* 150:695–706. <http://dx.doi.org/10.1083/jcb.150.4.695>
- Stutz, F., A. Bachi, T. Doerks, I.C. Braun, B. Séraphin, M. Wilm, P. Bork, and E. Izaurralde. 2000. REF, an evolutionary conserved family of hnRNP-like proteins, interacts with TAP/Mex67p and participates in mRNA nuclear export. *RNA.* 6:638–650. <http://dx.doi.org/10.1017/S1355838200000078>
- Tran, E.J., Y. Zhou, A.H. Corbett, and S.R. Wentz. 2007. The DEAD-box protein Dbp5 controls mRNA export by triggering specific RNA:protein remodeling events. *Mol. Cell.* 28:850–859. <http://dx.doi.org/10.1016/j.molcel.2007.09.019>
- Tuck, A.C., and D. Tollervey. 2013. A transcriptome-wide atlas of RNP composition reveals diverse classes of mRNAs and lncRNAs. *Cell.* 154:996–1009. <http://dx.doi.org/10.1016/j.cell.2013.07.047>
- Tutucci, E., and F. Stutz. 2011. Keeping mRNPs in check during assembly and nuclear export. *Nat. Rev. Mol. Cell Biol.* 12:377–384. <http://dx.doi.org/10.1038/nrm3119>
- Watzel, G., and W. Tanner. 1989. Cloning of the glutamine:fructose-6-phosphate amidotransferase gene from yeast. Pheromonal regulation of its transcription. *J. Biol. Chem.* 264:8753–8758.
- Wente, S.R., and M.P. Rout. 2010. The nuclear pore complex and nuclear transport. *Cold Spring Harb. Perspect. Biol.* 2:a000562. <http://dx.doi.org/10.1101/cshperspect.a000562>